Aging Behavior of Al- and Ga- Stabilized $Li_7La_3Zr_2O_{12}$ Garnet-Type, Solid-State Electrolyte Based on Powder and Single Crystal X-ray Diffraction

Günther J. Redhammer [1],*, **Gerold Tippelt** [1], **Andreas Portenkirchner** [1] and **Daniel Rettenwander** [2,3]

[1] Department of Chemistry & Physics of Materials, University of Salzburg, Jakob-Haringerstr. 2A, 5020 Salzburg, Austria; gerold.tippelt@sbg.ac.at (G.T.); andreas.portenkirchner@stud.sbg.ac.at (A.P.)

[2] Department of Material Science and Engineering, NTNU Norwegian University of Science and Technology, 7491 Trondheim, Norway; daniel.rettenwander@ntnu.no

[3] International Christian Doppler Laboratory for Solid-State Batteries, NTNU Norwegian University of Science and Technology, 7491 Trondheim, Norway

* Correspondence: guenther.redhammer@sbg.ac.at

Abstract: $Li_7La_3Zr_2O_{12}$ garnet (LLZO) belongs to the most promising solid electrolytes for the development of solid-state Li batteries. The stability of LLZO upon exposure to air is still a matter of discussion. Therefore, we performed a comprehensive study on the aging behavior of Al-stabilized LLZO (space group (SG) $Ia\bar{3}d$) and Ga-stabilized LLZO (SG $I\bar{4}3d$) involving 98 powder and 51 single-crystal X-ray diffraction measurements. A Li^+/H^+ exchange starts immediately on exposure to air, whereby the exchange is more pronounced in samples with smaller particle/single-crystal diameter. A slight displacement of Li from interstitial Li2 (96h) toward the regular tetrahedral Li1 (24d) sites occurs in Al-stabilized LLZO. In addition, site occupancy at the 96h site decreases as Li^+ is exchanged by H^+. More extensive hydration during a mild hydrothermal treatment of samples at 90 °C induces a structural phase transition in Al-LLZO to SG $I\bar{4}3d$ with a splitting of the 24d site into two independent tetrahedral sites (i.e., 12a and 12b), whereby Al^{3+} solely occupies the 12a site. Li^+ is preferably removed from the interstitial 48e site (equivalent to 96h). Analogous effects are observed in Ga-stabilized LLZO, which has SG $I\bar{4}3d$ in the pristine state.

Keywords: LLZO solid-state electrolyte; prolonged aging; Li^+-H^+ cation exchange; structural phase transition; single-crystal X-ray diffraction

1. Introduction

$Li_7La_3Zr_2O_{12}$ garnet (LLZO) belongs to the most promising group of solid electrolytes in the development of solid-state Li batteries (SSLBs), due to their superior high Li-ion conductivity of up to approximately 1 mS cm^{-1} at room temperature combined with its nonflammability, high chemical, and electrochemical stability, and its mechanical robustness [1,2].

The high Li-ion conductivity is associated with its cubic $Ia\bar{3}d$ structure, which can be stabilized by substituting Li at the tetrahedral side with aliovalent cations such as Al^{3+} [3] and introducing Li-disorder. Endmember LLZO itself is tetragonal, has a space group $I4_1/acd$, and has distinctly lower Li-ion conductivity [4]. Hence, a large body of work has focused on stabilizing the cubic modification by replacing Li^+ with e.g., Al^{3+}, Ga^{3+}, Fe^{3+} ([5–10] and references therein).

Although LLZO was originally assumed to be chemically stable during atmospheric exposure [11], it is now well established that it is sensitive to moisture, and spontaneous Li^+/H^+ exchange takes place while the garnet framework retains its structural stability [12–14]. Interestingly, its Li-ion conductivity decreases when exposed to humidity and air [15]. Overall, the structural alterations and associated changes in properties in Li-oxide garnets are strongly related to their composition. For example, Galven et al. [16]

demonstrated that instability of $Li_7La_3Sn_2O_{12}$ in a humid atmosphere, leading to protonated garnets $Li_{7-x}H_xLa_3Sn_2O_{12}$, is associated with a change in space group symmetry from tetragonal to cubic, while for $Li_{5-x}H_xLa_3Nb_2O_{12}$, the symmetry changed from tetragonal to a non-centrosymmetric cubic space group ($I2_13$). For tetragonal LLZO, Larraz et al. [17] found a transformation from tetragonal to the cubic modification at high temperatures (T_c ~645 °C) only when it is completely shielded from any humidity, and that the appearance of a lower temperature cubic phase between 100 and 200 °C occurs in the presence of water either in the immediate environment or in the sample itself. The same workers also observed the formation of a cubic form of LLZO during prolonged heating of pure tetragonal LLZO at around 350 °C in air and interpreted it to be the result of Li^+/H^+ exchange based on thermal analysis and Raman spectroscopy [17]. Later, Orera et al. [18] further attributed this structural change in pure tetragonal LLZO to Li^+/H^+ exchange and found two different cubic phases. Deep hydration led to a non-centrosymmetric $I\bar{4}3d$ phase where Li is mainly exchanged at the general 48*e* octahedral site and the two distinct tetrahedral sites have very different occupancies. In this structure, the protons are described as being located close to the O_2 oxygen atom based on powder neutron diffraction. Annealing above 300 °C resulted in a second, more 'normal' garnet structure, $Ia\bar{3}d$, with lower Li contents at the general 96*h* position (with octahedral coordinated Li^+). Table 1 summarizes the crystallographic positions, their Wykoff numbers, and multiplicities within the two main garnet structure types.

Table 1. Comparison of crystallographic positions in garnets with typical $Ia\bar{3}d$ [19] and acentric $I\bar{4}3d$ symmetry.

Space Group Symmetry		Coordination	Ion in LLZO
$Ia\bar{3}d$	$I\bar{4}3d$		
24*c*	24*d*	8	La^{3+}
16*a*	16*c*	6	Zr^{4+}
24*d*	12*a*	4	Li^+, Al^{3+}, Ga^{3+}
	12*b*	4	Li^+
96*h*	48*e*	4 + 2	Li^+
96*h*	48*e*		O^{2-}
	48*e*		O^{2-}

　　Uhlenbruck et al. [20] found that LLZO garnets react with water and carbon dioxide even at low concentrations of these reactants, e.g., when LLZO is stored in a glove box. They state that a fast-initial reaction of LLZO with moisture takes place, presumably by Li^+/H^+ exchange, and is accompanied by the formation of LiOH and Li_2CO_3. An increase in the lattice parameters is proposed by Galven et al. [21] to be caused by the replacement of stronger Li–O bonds by much weaker O–H . . . O bonds. This is supported by recent DFT calculations by Liu et al. [22]. For Ta-stabilized LLZO (nominally $Li_{6.6}La_3Zr_{0.6}Ta_{0.4}O_{12}$), the uptake of H^+ was systematically studied by immersing powders and pellets in water over a period of 7 days and a successive increase of unit cell dimensions of up to 0.115 Å, associated with a loss of 3.45 formula units of Li^+, was detected but with no change in space group symmetry was detected [23]. For Al-stabilized LLZO, excellent stability of the cubic $Ia\bar{3}d$ symmetry is reported at a wide range of pH conditions and under high Li^+/H^+ exchange rates of 63.6% [14]; no indications were found for a transformation to either $I\bar{4}3d$ or $I2_13$ symmetry using STEM and selected area electron diffraction (SAED). Later authors also note that even if the material undergoes deep hydration, there is no severe conductivity degradation. $Li_{6.25-x}H_xAl_{0.25}La_3Zr_2O_{12}$ retains its $Ia\bar{3}d$ symmetry after a moderate degree of ion exchange (~60% and lower), while intensive exchange reduces its symmetry to $I\bar{4}3d$ [22]. Using neutron diffraction data, the structure of the latter phase was refined with the assumption that there was full extraction of Li from the general 48*e* sites

and Al was equally distributed over both distinct tetrahedral sites, 12*a* and 12*b*, but more Li was extracted from the 12*a* site with Li$^+$ site occupancies of 0.34 (6) and 0.63 (7), respectively. It should be noted that contrary to arguments of Liu et al. [22] that the structural change is not visualized directly in the Bragg peaks, there are some weak characteristic reflections, which mark the transition: most obvious (but low in intensity) are the (3 1 0) and (7 1 0) peaks (at ~21.8° and 50.7° 2θ for Cu Kα radiation). Also, the equal distribution of Al over 12*a* and 12*b* sites need further clarification as it is known from Ga- and Fe-substituted LLZO material that the trivalent substituents show a preference for the 12*a* site. Nevertheless, the work of Liu et al. [22] gives the first report of non-centrosymmetric space group $I\bar{4}3d$ in deeply hydrated Al-stabilized LLZO material (H-LLZO). Based on inelastic neutron scattering data, they propose that it is primary H$^+$, not H$_3$O$^+$, which is present in H-LLZO. Very recently, Redhammer et al. [24] investigated the stability of Ta-substituted LLZO (Li$_6$La$_3$ZrTaO$_{12}$) under wet environments and mild hydrothermal conditions and, indeed, they observed a structural phase transition to the $I\bar{4}3d$ symmetry under deep hydration conditions, accompanied by distinct increases in lattice parameters and loss of Li$^+$ mainly at the 96*h* and 48*e* positions.

Hiebl et al. [25] studied the proton bulk diffusion in Al stabilized cubic Li$_{6.4}$La$_3$Zr$_2$Al$_{0.2}$O$_{12}$ using single-crystal X-ray diffraction by remeasuring the same crystal over a period of more than two years. They found a rapid increase in the lattice parameters in the first weeks accompanied by a loss of Li$^+$, especially at the 96*h* position of the garnet structure. However, the data density is low especially within the first period of aging.

Herein, we thus focused on the first weeks of aging in humid air, again using single-crystal X-ray diffraction. We also extend our investigations to consider aging under mild hydrothermal conditions to induce deeper hydration and document any associated change in symmetry. The main aims are to systematically monitor the loss of Li$^+$ during aging, to determine which Li-position is more accessible for extraction, especially within the non-centrosymmetric $I\bar{4}3d$ phase, and to look at any small structural changes, which might be associated with the Li$^+$/H$^+$ exchange. The results are compared with the behavior of aging Ga-stabilized LLZO, the latter being in $I\bar{4}3d$ symmetry already in the pristine state. Finally, the aging of polycrystalline powders of both compounds are also investigated under different conditions (dry and humid air, water). The use of single-crystal X-ray diffraction here is superior to powder X-ray diffraction, as high resolution 3-dimensional reciprocal space data are necessary to detect unambiguous symmetry changes, small structural alterations upon Li$^+$/H$^+$ exchange, and site occupation numbers.

2. Materials and Methods

2.1. Synthesis

Coarse-grained sample material, suitable for single-crystal X-ray diffraction work, was prepared by a solid-state ceramic sintering route as described in detail in [7,26]. Li$_2$CO$_3$ (99%, Merck, Darmstadt, Germany; with a 10% excess), La$_2$O$_3$ (99.99%, Roth, Karlsruhe, Germany, preheated at 800 °C for 12 h), ZrO$_2$ (99.5%, Roth, Karlsruhe, Germany), and Al$_2$O$_3$ or Ga$_2$O$_3$ (99.8%, Aldrich, Darmstadt, Germany) were mixed in the required stoichiometry for the nominal compositions Li$_{6.7}$La$_3$Zr$_2$Al$_{0.1}$O$_{12}$ (Al10-LLZO), Li$_{6.7}$La$_3$Zr$_2$Ga$_{0.1}$O$_{12}$ (Ga10-LLZO) and Li$_{5.8}$La$_3$Zr$_2$Ga$_{0.4}$O$_{12}$ (Ga40-LLZO), and uniaxially cold-pressed to pellets. Green pellets were fired in the air at 850 °C using an open corundum crucible for 4 h in a muffle furnace to ensure decarbonatization. After carefully regrinding the pellets using an agate mortar, the material was subsequently ball-milled for 1 h in isopropyl alcohol (Pulverisette 7, Fritsch GmbH, Idar-Oberstein, Germany, 800 rpm, 2 mm ZrO$_2$ balls). After drying in air, the milled powders were again pelletized and sintered at 1230 °C at a heating/cooling rate of 5 K/min and held at maximum temperature for 6 h with a sacrificial LLZO pellet above and below the sample to hinder Li loss during sintering and uptake of Al from the alumina crucibles. For these buffer pellets, the calcinated material was hand-milled, pressed, and sintered a second time at 1050 °C for 18 h.

Single crystals were selected from the freshly prepared and sintered ceramic pellets immediately on cooling and first measured within 6 h after synthesis. Powdered material of the pristine sintered pellets were also characterized for their phase purity, and lattice parameters were evaluated with powder X-ray diffraction experiments immediately after they were removed from the furnace. Unused material was sealed in plastic containers and stored under Argon atmosphere in a glove box.

2.2. X-ray Powder Diffraction

Powder X-ray diffraction data were collected at room temperature in coupled θ-θ mode on a Bruker D8 Advance instrument with a DaVinci-Design diffractometer (Bruker AXS, Karlsruhe, Germany), using a fast-solid state Lynxeye detector (Bruker AXS, Karlsruhe, Germany). Data acquisition used Cu $K_{\alpha1,2}$ radiation between 5° and 110° 2θ, with a step size of 0.015°, the integration time of 1 s, and the divergence- and anti-scatter-slits open at 0.3° and 4° respectively. A primary and secondary side 2.5° soller slit was used to minimize axial divergence, and the detector window opening angle was set at 2.93°. For data collection, all samples were prepared on single-crystal silicon zero-background sample holders. Data was assessed with TOPAS^{TM} 4.2 [26]; here, the background was modeled with a Chebychev function of 5th order, and a fundamental parameter approach was used to describe the peak shape of the Bragg reflections. Starting models for the garnet phases in Rietveld refinements were taken from [7,9].

2.3. Aging Experiments

Immediately after the synthesis, parts of the pellets of Ga- and Al-stabilized LLZO were carefully ground to a fine powder in an agate mortar under dry conditions before initial diffraction experiments were carried out. The as-prepared samples for XRPD (thin powder film smeared onto silicon—zero background sample holders) were kept under laboratory conditions (22.0(3) °C, air moisture 15–20%) and measured from time to time from day 0 (first measurement for Ga and Al—stabilized LLZO) to the 632nd or 633th day thereafter. The second set of samples, prepared on standard silicon—zero background sample holders, was kept in a closed desiccator-the bottom filled with distilled water so that these two samples were undersaturated water vapor pressure at 22.0(3) °C. Again, they were measured from time to time over the same period.

The remaining powder was used for additional aging experiments: 50 mg of the stabilized LLZO material was immersed in 250 mL of de-ionized water in a glass beaker, shut with parafilm, and regularly shaken to homogenize the material. The pH value was measured at different stages of aging: it increased immediately upon adding the LLZO powders from 6.8 to ~12 but remained almost constant thereafter. There was no evolution of gas when immersion the LLZO into the water. The aged samples were filtered and dried under vacuum and immediately analyzed with powder X-ray diffraction to monitor any changes in cell parameters.

Finally, parts of the initial pellets were gently crushed. Care was taken not to destroy the formed, small, single crystals. This crushed material was used for both aging experiments in water (50 mg of sample material to 100 mL liquid) and the mild hydrothermal treatment. For the latter, about 50 mg of the sample together with 15 mL of distilled water were put in a 45 mL Teflon lined and tightly closed steel autoclave and kept at 90 °C in a drying chamber for up to 14 days. Generally, the aging experiments were started within one day after the end of the synthesis. Where this was not possible (aging of small single crystals), uncrushed pellets were packed under Argon and kept in a glove box until use and stored for no longer than 4 weeks. The methodology of aging is very similar to that used for $Li_6La_3TaZrO_{12}$ [24].

2.4. Single Crystal X-ray Diffraction

For single-crystal X-ray diffraction (SCXRD), two suitable crystals selected based on their optical properties (regular shape and homogeneity in color), were glued onto glass

capillaries (0.1 mm Ø); excess glue was carefully removed from the surface with acetone to maximize the area of the crystals' surface exposed to air. After a first measurement, the two single crystals were stored on the pin in a desiccator. Instead of the drying agent, the desiccator was filled with water so that a saturated water vapor atmosphere was achieved and maintained at 22 °C (lab conditions) over the entire period of observation. The integrity of both crystals is maintained over the whole period, based on optical inspection and the sharpness of observed Bragg peaks.

Single-crystal X-ray diffraction data were collected on a SMART APEX CCD-diffractometer (Bruker AXS, Karlsruhe, Germany). Intensity data were collected with a graphite-monochromatized Mo K_α X-radiation source (50 kV, 20 mA); the crystal-to-detector distance was 30 mm and the detector was positioned at $-30°$ and $-50°$ 2θ and an ω-scan mode strategy were applied at four different φ positions ($0°$, $90°$, $180°$, and $270°$) for each 2θ position. A total of 630 frames with $\Delta\omega = 0.3°$ were acquired for each run. With this strategy, data could be acquired over a large q-range, up to minimum d-values of $d = 0.53$ Å. This is necessary for the accurate determination of anisotropic displacement parameters and to reduce correlation effects between atomic displacement parameters and site occupation numbers. Three-dimensional data were integrated and corrected for Lorentz-, polarization and background effects using the APEX3 software [27]. Structure solution (using direct methods) and subsequent weighted full-matrix least-squared refinements on F^2 were done with SHELX-2012 [28] as implemented in the program suite WinGX 2014.1 [29]. Experimental and refinement parameters for a selected set of data are given in Table 2, and the corresponding fractional atomic coordinates and equivalent isotropic displacement parameters are collated in Table 3, selected bond lengths can be found in Table 4, Table 5 gives refined site occupation numbers. Note, data for these refinements are deposited at the Cambridge Crystal Data Center CCDC under CSD numbers 2086964–2086969.

Table 2. Experimental details and refinement results of X-ray diffraction data of selected stabilized LLZO single crystals; Experiments were carried out with Mo Kα—Radiation and $\lambda = 0.71073$ Å using a Bruker Smart Apex 3-circle diffractometer. Full-matrix least-square refinement of F^2.

	Al-LLZO Pristine	Al-LLZO 969 d Air	Al-LLZO Hydro-9d	Ga-LLZO Pristine	Ga-LLZO 859 d Air	Ga-LLZO Hydro-28d
			Crystal data			
Crystal system	cubic	cubic	cubic	cubic	cubic	cubic
Space group	$Ia\bar{3}d$	$Ia\bar{3}d$	$I\bar{4}3d$	$I\bar{4}3d$	$I\bar{4}3d$	$I\bar{4}3d$
Z	8	8	8	8	8	8
a (Å)	12.9629 (2)	12.9806 (2)	13.0057 (2)	12.9668 (7)	12.9741 (2)	13.0460 (2)
V (Å^3)	2178.24 (10)	2184.18 (6)	2199.89 (10)	2180.2 (4)	2183.89 (10)	2220.40 (10)
Density mg/m^3	5.052	4.988	4.974	5.084	5.059	5.000
μ (mm^{-1})	13.253	13.254	13.254	13.531	13.543	13.897
Crystal Size (mm)	0.12	0.12	0.13	0.14	0.14	0.08
	0.11	0.11	0.12	0.12	0.12	0.07
	0.08	0.08	0.07	0.12	0.12	0.04
			Data Collection			
$(sin\theta/\lambda)_{max}$ (Å^{-1})	0.838	0.839	0.812	0.700	0.839	0.834
Reflections coll.	33,003	32,869	34,671	4101	34,741	35,386
Independ. Refl.	455	459	835	514	908	910
Index Ranges: h	$-21 \ldots 21$	$-21 \ldots 21$	$-21 \ldots 21$	$-17 \ldots 12$	$-21 \ldots 21$	$-21 \ldots 21$
k	$-21 \ldots 21$	$-21 \ldots 21$	$-21 \ldots 21$	$-17 \ldots 16$	$-21 \ldots 21$	$-21 \ldots 21$
l	$-21 \ldots 21$	$-21 \ldots 21$	$-21 \ldots 21$	$-14 \ldots 9$	$-21 \ldots 21$	$-21 \ldots 21$
R_{int}	2.98	2.62	3.67	2.42	2.21	3.11

Table 2. *Cont*.

	Al-LLZO Pristine	Al-LLZO 969 d Air	Al-LLZO Hydro-9d	Ga-LLZO Pristine	Ga-LLZO 859 d Air	Ga-LLZO Hydro-28d
Refinement						
Data	455	459	835	514	908	910
Restrains	0	1	1	1	1	3
Parameters	30	29	43	42	42	44
R1 (all data)	1.72	2.55	1.91	1.56	1.79	2.88
wR2 (all data)	3.18	4.50	3.32	2.91	3.84	6.10
Goodness of Fit	1.545	1.418		1.191	1.412	1.498
$\Delta\rho_{max}$, $\Delta\rho_{min}$ (e/Å)	0.638, −0.399	0.822, −0.849	0.535, −0.798	0.458, −0.428	0.666, −0.790	1.213, −1.316

Table 3. Fractional atomic coordinates, site occupation factors (sof), and equivalent isotropic atomic displacement parameters U_{eq} for the Al- and Ga-stabilized LLZO samples are listed in Table 2.

Atom	Site	x	y	z	occ	U_{eq}
Al-LLZO, pristine						
La1	24c	0.125	0	0.25	0.2461 (7)	0.00871 (8)
Zr1	16a	0	0	0	0.16667	0.00674 (12)
O1	96h	0.0999 (13)	0.19601 (13)	0.28187 (13)	1	0.0118 (3)
Li1	24d	0.375	0	0.25	0.1025 (14)	0.0173 (7)
Al1	24d	0.375	0	0.25	0.0125	0.017 (5)
Li2	96h	0.0939 (12)	0.1890 (12)	0.4241 (11)	0.375 (2)	0.028 (5)
Al-LLZO, air 936d						
La1	24c	0.125	0	0.25	0.2473 (11)	0.01115 (11)
Zr1	16a	0	0	0	0.16667	0.00994 (18)
O1	96h	0.10044 (18)	0.1954 (2)	0.2813 (2)	1	0.0133 (4)
Li1	24d	0.375	0	0.25	0.148 (2)	0.038 (9)
Al1	24d	0.375	0	0.25	0.013 (2)	0.038 (9)
Li2	96h	0.1016 (18)	0.1871 (21)	0.4263 (21)	0.234 (3)	0.013 (7)
Al-LLZO, hydro 9d						
La1	24d	0.12389 (4)	0	0.25	0.4979 (7)	0.01305 (6)
Zr1	16c	−0.00275 (4)	−0.00275 (4)	−0.00275 (4)	0.33333	0.0123 (1)
O1	48e	0.0992 (3)	0.1937 (3)	0.2787 (3)	1	0.0179 (8)
O2	48e	0.0327 (3)	0.4450 (3)	0.1481 (3)	1	0.01544 (7)
Li1	12a	0.375	0	0.25	0.187 (2)	0.044 (9)
Al1	12a	0.375	0	0.25	0.025 *	0.044 (9)
Li2	12b	0.875	0	0.25	0.191 (19)	0.032 (7)
Li3	48e	0.110 (3)	0.188 (3)	0.425 (3)	0.214 (3)	0.02 *
H1	48e	0.136 (5)	0.189 (5)	0.289 (5)	0.90508	0.02 *
Ga-LLZO, pristine						
La1	24d	0.12056 (3)	0	0.25	0.4922 (14)	0.00673 (14)
Zr1	16c	−0.00019 (4)	−0.00019 (4)	−0.00019 (4)	0.33333	0.0054 (2)
O1	48e	0.0976 (3)	0.1965 (3)	0.2803 (3)	1	0.0097 (8)
O2	48e	0.0333 (3)	0.4447 (3)	0.1474 (3)	1	0.0114 (8)
Li1	12a	0.375	0	0.25	0.1891 (7)	0.0059 (18)
Ga1	12a	0.375	0	0.25	0.0209 (7)	0.0059 (18)
Li2	12b	0.875	0	0.25	0.187 (3)	0.023 (9)
Li3	48e	0.0964 (9)	0.1870 (10)	0.4248 (11)	0.610 (4)	0.010 (5)

Table 3. *Cont.*

Atom	Site	x	y	z	occ	U_{eq}
			Ga-LLZO, air 836 d			
La1	24*d*	0.12156 (3)	0	0.25	0.4938 (17)	0.00869 (9)
Zr1	16*c*	0.00066 (4)	0.00066 (4)	0.00066 (4)	0.33333	0.00731 (15)
O1	48*e*	0.0989 (3)	0.1963 (3)	0.28051 (3)	1	0.0112 (7)
O2	48*e*	0.0322 (3)	0.4442 (3)	0.1477 (3)	1	0.0113 (6)
Li1	12*a*	0.375	0	0.25	0.2208 (8)	0.0098 (14)
Ga1	12*a*	0.375	0	0.25	0.0202 (8)	0.0098 (14)
Li2	12*b*	0.875	0	0.25	0.138 (4)	0.049 (2)
Li3	48*e*	0.0987 (12)	0.1878 (13)	0.4260 (13)	0.506 (6)	0.011 (4)
			Ga-LLZO, hydro 28d			
La1	24*d*	0.12077 (6)	0	0.25	0.498 (3)	0.01183 (14)
Zr1	16*c*	−0.00344 (8)	−0.00344 (8)	−0.00344 (8)	0.33333	0.0123 (3)
O1	48*e*	0.0991 (5)	0.1931 (5)	0.2775 (5)	1	0.0118 (11)
O2	48*e*	0.0332 (6)	0.4448 (6)	0.1467 (5)	1	0.0144 (12)
Li1	12*a*	0.375	0	0.25	0.1956 (9)	0.0132 (13)
Ga1	12*a*	0.375	0	0.25	0.0544 (9)	0.0132 (13)
Li2	12*b*	0.875	0	0.25	0.101 (3)	0.007 (6)
Li3	48*e*	0.096 (5)	0.195 (6)	0.432 (6)	0.147 (5)	0.01 *
H1	48*e*	0.122 (11)	0.175 (10)	0.324 (8)	0.84 (2)	0.01 *

* = value fixed during refinement.

Table 4. Selected bond lengths for the Al- and Ga-stabilized LLZO samples are listed in Table 2.

Al-LLZO-Pristine			
La1—O1 [i]	2.5104 (17)	Li2—Li2 [vii]	0.85 (3)
La1—O1 [ii]	2.5947 (17)	Li2—O1	1.848 (15)
Zr1—O1 [iii]	2.1086 (16)	Li2—O1 [ix]	2.064 (16)
Li1—Li2 [iv]	1.585 (19)	Li2—O1 [vii]	2.182 (16)
Li1—O1 [v]	1.9038 (17)	Li2—O1 [x]	2.224 (16)
Li1—Li2 [vi]	2.398 (19)		
Al-LLZO-969d-air			
La1—O1 [i]	2.513 (3)	Li2—Li2 [vii]	0.64 (4)
La1—O1 [ii]	2.588 (3)	Li2—O1 [i]	1.88 (2)
Zr1—O1 [iii]	2.106 (2)	Li2—O1 [vii]	2.13 (3)
Li1—Li2 [iv]	1.69 (2)	Li2—O1 [ix]	2.16 (2)
Li1—O1 [v]	1.919 (3)	Li2—O1 [x]	2.27 (3)
Li1—Li2 [vi]	2.30 (2)		
Al-LLZO-Hydro-9d			
La1—O1 [i]	2.502 (4)	Li2—O2 [xiv]	1.925 (4)
La1—O2 [xi]	2.533 (4)	Li2—Li3 [xv]	2.22 (4)
La1—O1	2.566 (4)	Li3—O1	1.91 (4)
La1—O2 [i]	2.591 (4)	Li3—O2 [i]	2.09 (4)
Zr1—O1 [xii]	2.088 (4)	Li3—O1 [x]	2.30 (4)
Zr1—O2 [xiii]	2.137 (4)	Li3—O1 [ix]	2.30 (4)
Li1—Li3 [iv]	1.77 (4)	Li3—O2 [ix]	2.58 (4)
Li1—O1 [v]	1.941 (4)		

Table 4. *Cont.*

Ga-LLZO-pristine			
La1—O2 ^{xi}	2.504 (4)	Li2—O2 ^{xiv}	1.923 (4)
La1—O1 ^{i}	2.524 (4)	Li2—Li3 ^{xv}	2.359 (13)
La1—O2 ^{i}	2.584 (4)	Li3—O1	1.878 (13)
La1—O1	2.595 (4)	Li3—O1 ^{ix}	2.079 (14)
Zr1—O2 ^{xiii}	2.089 (4)	Li3—O2 ^{i}	2.115 (14)
Zr1—O1 ^{xii}	2.129 (4)	Li3—O1 ^{x}	2.232 (14)
Li1—Li3 ^{iv}	1.627 (13)	Li3—O2 ^{ix}	2.662 (14)
Li1—O1 ^{v}	1.895 (4)		
Ga-LLZO-859d-air			
La1—O2 ^{xi}	2.503 (4)	Li2—O2 ^{xiv}	1.932 (4)
La1—O1 ^{i}	2.527 (4)	Li2—Li3 ^{xv}	2.332 (16)
La1—O2 ^{i}	2.577 (4)	Li3—O1	1.891 (18)
La1—O1	2.594 (4)	Li3—O1 ^{ix}	2.110 (17)
Zr1—O2 ^{xiii}	2.082 (4)	Li3—O2 ^{i}	2.130 (17)
Zr1—O1 ^{xvii}	2.127 (4)	Li3—O1 ^{x}	2.243 (18)
Li1—Li3 ^{iv}	1.652 (16)	Li3—O2 ^{ix}	2.631 (17)
Li1—O1 ^{v}	1.906 (4)		
Ga-LLZO-Hydro28d			
La1—O2 ^{xi}	2.523 (7)	Li2—O2 ^{xiv}	1.942 (7)
La1—O1 ^{i}	2.531 (6)	Li2—Li3 ^{xv}	2.38 (7)
La1—O1	2.560 (7)	Li3—O1	2.02 (7)
La1—O2 ^{i}	2.600 (7)	Li3—O1 ^{x}	2.14 (8)
Zr1—O1 ^{xii}	2.085 (7)	Li3—O1 ^{ix}	2.15 (7)
Zr1—O2 ^{xiii}	2.138 (6)	Li3—O2 ^{i}	2.22 (8)
Li1—Li3 ^{iv}	1.62 (7)	Li3—O2 ^{ix}	2.60 (7)
Li1—O1 ^{v}	1.960 (6)		

Symmetry code(s): (i) z, x, y; (ii) $x, -y, -z + 1/2$; (iii) $-y + 1/4, -x + 1/4, -z + 1/4$; (iv) $-z + 3/4, y - 1/4, -x + 1/4$; (v) $-z + 3/4, -y + 1/4, x + 1/4$; (vi) $y + 1/4, -x + 1/4, z - 1/4$; (vii) $-x + 1/4, z - 1/4, y + 1/4$; (viii) y, z, x; (ix) $y - 1/4, -x + 1/4, -z + 3/4$; (x) $-y + 1/4, x + 1/4, -z + 3/4$; (xi) $-x, -y + 1/2, z$; (xii) $y - 1/4, x - 1/4, z - 1/4$; (xiii) $z, -x, -y + 1/2$; (xiv) $x + 3/4, z - 1/4, y - 1/4$; (xv) $y + 3/4, x - 1/4, z - 1/4$; (xvi) $-y + 1/4, x - 3/4, -z + 3/4$; (xvii) $x - 1/4, z - 1/4, y - 1/4$.

Table 5. Refined site occupation numbers (per Formula Unit; pfu) of Al- and Ga- stabilized LLZO for the samples listed in Table 2.

Sample ID	S.G.	La	Zr	Li1	Li2	Li3	Δ Li
Al-LLZO, pristine	$Ia\bar{3}d$	2.95 (2)	2.0	1.23 (4)	4.51 (4)	–	–
Al-LLZO, 936d air		2.97 (4)	2.0	1.78 (3)	2.81 (4)	–	1.15
Al-LLZO, hydro 9d	$I\bar{4}3d$	2.99 (2)	2.0	1.12 (2)	1.15 (2)	1.29 (4)	3.47
Ga-LLZO, pristine	$I\bar{4}3d$	2.94 (2)	2.0	0.93 (2)	0.98 (2)	4.00 (4)	–
Ga-LLZO, 859d	$I\bar{4}3d$	2.96 (2)	2.0	1.33 (2)	0.83 (2)	3.04 (4)	0.71
Ga-LLZO, hydro 28d	$I\bar{4}3d$	2.98 (3)	2.0	0.94 (4)	0.61 (4)	0.88 (5)	3.48

3. Results and Discussion

3.1. Synthesis and Powder X-ray Diffraction (PXRD)

Sintered pellets of both Al- and Ga- stabilized LLZO appear dense and homogenous in color. On sintering at 1230 °C, the pellets significantly have shrunk and small single crystals are visible on the surfaces and inside the pellets under an optical microscope (Figure 1). The crystallite sizes range up to 150 μm and are, thus, suitable for single crystal work.

Buffer pellets retained their size, probably resulting from a different milling procedure, i.e., this material was not ball-milled.
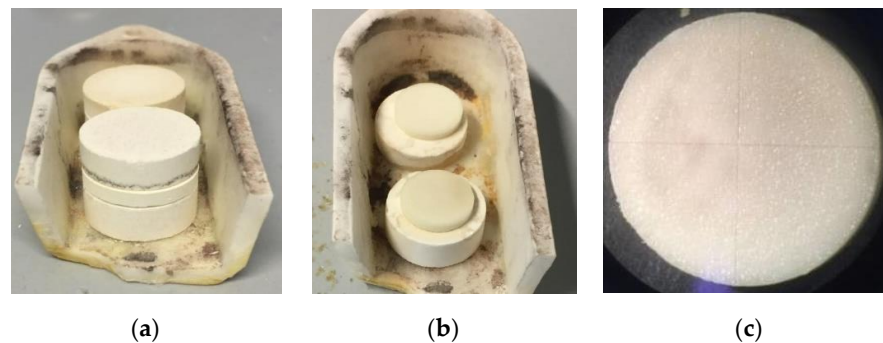

(**a**)	(**b**)	(**c**)

Figure 1. Pellets of Ga40-LLZO before (**a**) and after (**b**) the final sintering step at 1230 °C, the top and bottom pellets are buffer pellets of the same composition. (**c**) A pellet of Ga40-LLZO under a stereo-loupe; note, the diameter of the pellet is 8 mm.

In PXRD, both synthesized compositions appear to be a perfect single phase with sharp diffraction lines, and they can be indexed and refined based on the cubic $Ia\bar{3}d$ and $I\bar{4}3d$ space groups for Al- and Ga-stabilized LLZO, respectively. The lattice parameters of the two LLZO samples, determined directly after finishing the synthesis, are close to the ones reported in the literature [7,9].

During aging in air, lattice parameters generally expand, which is indicative of Li^+-H^+ exchange reaction as proposed in the literature [14,17,20,24,25,30]. In detail, individual peaks in the PXRD pattern of Al10-LLZO shift to lower Bragg angles (indicative of an increase in lattice parameters) with increased exposure to dry air. Some shoulders appear at the low angle sides of the peaks and small amounts of Li_2CO_3 appear, probably as a product of CO_2 in the air reacting with LiOH, which forms on the surface. This is shown for some selected aging times in Figure 2.
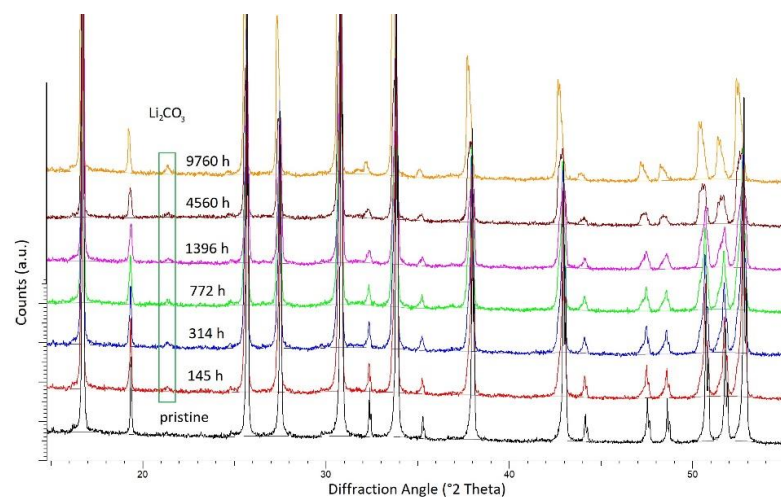
Figure 2. Sections of the powder X-ray diffraction pattern for Al20-LLZO aged in the air at different times. Note the increased amount of Li_2CO_3 and the development of a low angle shoulder, particularly visible at higher Bragg angles.

This development of low angle shoulders was not observed during the aging of $Li_6La_3ZrTaO_{12}$ garnet (LLZTO) in the air in the study of [24] but is evident in Al10-LLZO and Ga40-LLZO samples aged in air in this study. Data can be generally refined with a single garnet phase. However, there is a better fit using a two-garnet-phase refinement; one with extensive Li^+-H^+ exchange—most probably corresponding to surface alteration,

and another describing deeper material that had less direct contact to air. Figure 3a depicts the variation of lattice parameters for Al10-LLZO.
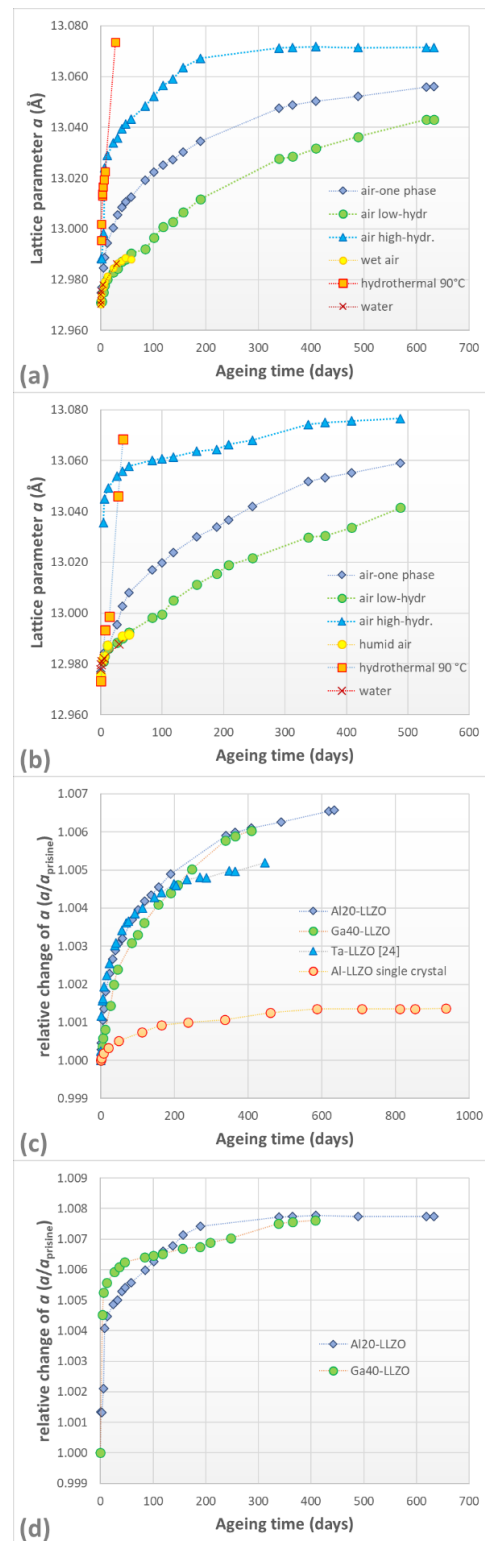

Figure 3. Variation in lattice parameters of (**a**) Al10-LLZO and (**b**) Ga40-LLZO under different aging conditions as a function of time (aging) in days. (**c**) Comparison of the relative changes in lattice parameters during aging in air with a one-garnet model. Data for $Li_6La_3ZrTaO_{12}$ from [24] are also included for comparison. (**d**) Relative changes in the highly hydrated surface material. Estimated standard deviations/error bars are smaller than the symbols.

From Figure 3a, it is evident that weathering starts immediately on exposure to air, even if the humidity is low. When using the one garnet model, the *a* lattice parameter increases by ~0.03 Å within the first month of observation. Applying the two-phase model, the increase of the exposed, surface material shows an increase of almost 0.065 Å in the same period. It is interesting to note that for this surface garnet phase, saturation takes place after ~300 days with a lattice parameter of around 13.072 Å, while the deeper material shows a steady increase.

In a humid atmosphere, Al10-LLZO shows no long-term stability. Sample aging is marked by proton incorporation with a sudden increase in lattice parameters within the first days of exposure and is similar to the behavior of the low-hydrated garnet phase in air. Li_2CO_3 is also formed. An additional, new phase appears after 5.8 days of aging; this phase could not be identified even after an intensive search of both the COD and the PDF databases. It is interesting to note that in the data sets collected after days 7 and 8, this phase has nearly all gone and is replaced by a Lanthanite (La) -type material, $La_2(CO_3)_3 \cdot 8H_2O$. Zr may be also incorporated into this phase as no Zr-containing phases could be identified. With time, both the unknown phase and the Lanthanite- (La) compound increase in abundance at the expense of Al-LLZO; after day 50 of exposure, no garnet phase is detected. It should be noted that no Li_2CO_3, LiOH, or $La(OH)_3$ phases are found in these phase mixtures. Therefore, the high moisture conditions promote the decomposition of the LLZO material and enhance the formation of a crystalline hydrated La-carbonate phase as well as another—unidentified—phase. Immersion of Al20-LLZO in distilled water has a similar effect as that in moist air, i.e., Li^+-H^+ ion-exchange drives a lattice parameter increase. However, no second garnet phase is detected and the data show changes similar to that of the weakly hydrated garnet upon exposure to air: no line broadening is observed. For the sample aged in water, it would appear that even the particle cores become highly hydrated such that they are readily dissolved in water, because X-ray diffraction of the solid residue left after the immersion water had evaporated on day 30 of aging, shows only Li_2CO_3 and $La(OH)_3$ remaining.

Also included in Figure 3a are data for the hydrothermally treated material at 90 °C. Here, lattice parameters suddenly increase and the data follows a similar trend to that shown by the surface-hydrated Al20-LLZO that was exposed to air. In the aging experiment, a lattice parameter value of $a = 13.0735$ (12) Å is reached after day 28 at 90 °C; this is the same order of magnitude observed during the weathering in air after ~300 days. Unfortunately, the single-crystal material in this experiment was completely fractured and no single crystals could be recovered from the remaining, fine-grained powder (~3 μm crystallites in size). It should be noted that no unequivocal evidence is found for two different phases in the hydrothermal experiments.

Figure 3b depicts the variations in lattice parameters for Ga40-LLZO during aging. Similar trends to Al10-LLZO are observed. The sample exposed to dry air again shows the development of shoulders and peak splitting at the low angle part of the Bragg-peaks and small amounts of Li_2CO_3 are formed already after about one week of air exposure, with the amount increasing with increasing exposure times (~14 wt.% after 488 days as determined from the Rietveld refinements). Near-surface material quickly takes up H^+ at a rate that is comparably faster than Al10-LLZO and reaches a plateau after ~350 days with unit cell dimensions of ~13.075 Å, i.e., somewhat larger than in Al10-LLZO. Exposure to saturated humid air causes quick decomposition of the material, with the first appearance of the unknown phase after day 4 and the formation of Lanthanite- (La) after day 5. No garnet phase could be detected after 45 days of weathering. In dry air (normal lab conditions), garnet remains stable, with some Li_2CO_3, after the entire period of observation of almost 3 years. Changes in the lattice parameter of the humid air-exposed samples and the material submerged in distilled water follow similar trends to those of the weakly hydrated material exposed to normal air. Effects from hydrothermal treatment at 90 °C are similar to those observed in Al10-LLZO: Li^+-H^+ exchange is enhanced, and the sample treated for 36 days

shows a lattice expansion to a = 13.0685 (1) Å. In addition to the garnet phase, La(OH)$_3$ was found in the dried residue.

The relative changes in lattice parameters of the one-garnet phase model for Al10-LLZO and Ga40-LLZO, relative to the pristine state, indicate an almost identical degree of expansion during aging for Li$_6$La$_3$ZrTaO$_{12}$ (LLZTO) and Al10-LLZO at short aging times (Figure 3c). However, after 150 days, the values flatten out more than for the other two compositions. Early H$^+$ uptake seems to be quicker in Al-stabilized material than in Ga-stabilized LLZO, but after long aging times, values almost overlap. However, when looking at the values for the surface material (Figure 3d), the trend seems to be reversed. Generally, obvious aging is fast in powders indicating that they are particularly sensitive to exposure to moisture, even at low humidity levels. The uptake of H$^+$ is also observed in the studied single crystals: rates of Li$^+$-H$^+$ exchange (Figure 3c) are much less due to distinctly larger crystallite sizes and diffusion paths are effectively much longer (see the following section).

3.2. Single Crystal X-ray Diffraction

It is now generally accepted that the increase in lattice parameters of LLZO-type material with time is due to weathering effects, and the main mechanism driving this is the uptake of H$^+$ into the structure at the expense of Li$^+$. However, the mechanisms for this Li$^+$-H$^+$ exchange, particularly which crystallographic sites are accessible and take part in the exchange, are still not well known. To the best of our knowledge, the work of [24] on Li$_6$La$_3$ZrTaO$_{12}$ is the only one and is based on experimental diffraction data on powders and especially on single—Crystals to resolve this issue. A similar approach is taken in this current study, with a full structural analysis on aged single crystals of Al- and Ga-stabilized LLZO, the former with space group symmetry $Ia\bar{3}d$ in the pristine state and independent of the degree of doping, and the latter with acentric space group $I\bar{4}3d$. The two Ga-LLZO samples used have nominal Ga-contents of 0.1 and 0.4 apfu and were chosen to reveal any possible effect of doping concentrations on aging.

3.2.1. Structural Analysis of Al-Stabilized LLZO

First, the effects of aging are reported for a single crystal, which was stored in the wet atmosphere in a desiccator. The same crystal was re-measured from time to time so that 15 data sets with maximum exposure to high moisture air of 936 days (~2 $\frac{1}{2}$ years) were obtained. The pristine sample and all of its repeated measurements reveal space group symmetry $Ia\bar{3}d$, i.e., no evidence for a change in symmetry is observed. Structure refinements converged to very low-reliability factors and anisotropic atomic displacement parameters could be determined for all atoms, except the Li2 site, see Tables 1 and 2.

The lattice parameters increase, especially within the first 100 days. However, the Li$^+$-H$^+$ exchange is distinctly slower than that in the powder material (cf. Figures 3c and 4a). The lattice parameter stabilizes to a value of ~12.9805 (2) Å after long exposure times. Data from Hiebl et al. [25] are included in Figure 4a and there is a good agreement between both data sets, with distinctly higher data density in the results of this study, so calculated trends will be more reliable. Generally, even short exposure to air induces some modification, which can be followed in a variation of the structural parameters.

The framework of the LLZO garnet structure in the $Ia\bar{3}d$ symmetry is built up of 8-fold oxygen coordinated dodecahedral sites that host the La^{3+}. In concordance with previous studies [7–9,24], a small deficit in site occupation is found. Zr^{4+} occupies the 16a sites with a regular 6-fold oxygen atom coordination. The edge-sharing octahedral and dodecahedral polyhedra build an open, integrated framework, in which the Li$^+$ atoms are located. As it was outlined by several authors [5–8,10,26], there are two positions, which host lithium, namely Li1 at special position 24d at ($^3/_8$, 0, $\frac{1}{4}$), corresponding to the regular tetrahedral position in the garnet structure, and interstitial general site 96h at ~(0.1, 0.18, 0.43). The $Ia\bar{3}d$ crystal structure is illustrated in Figure 5.

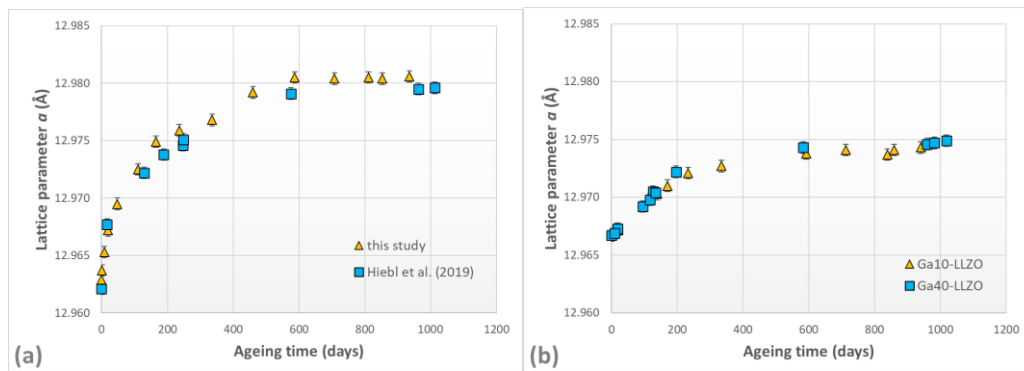**Figure 4.** Variation of lattice parameters of (**a**) the Al10-LLZO single crystal and (**b**) two different compositions of Ga^{3+} stabilized LLZO, exposed to humid air.
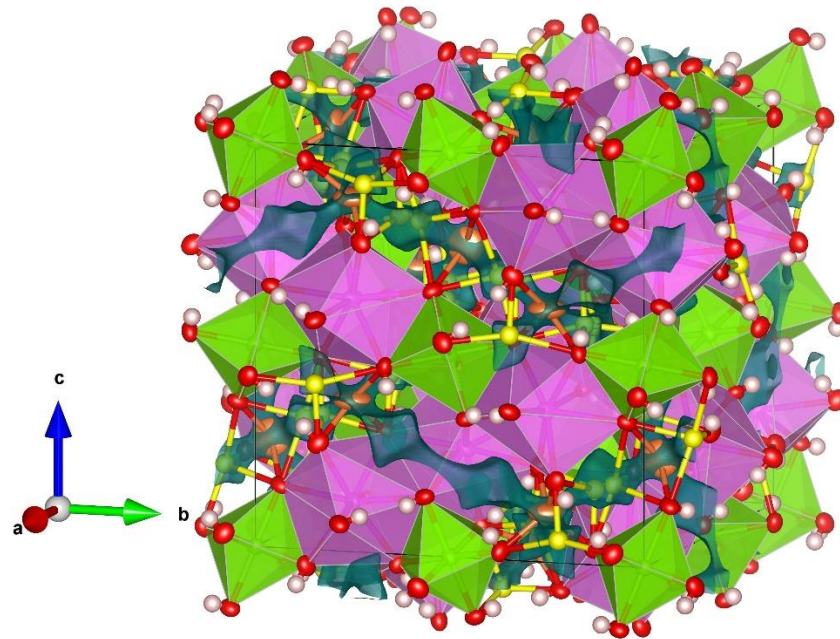

Figure 5. Crystal structure of Al10-LLZO, aged for 936 days, with the space group $Ia\bar{3}d$, in a polyhedral representation. LaO_8 sites appear in pink, ZrO_6 octahedra is yellowish-green. The Li(1) (orange) and Li(2) sites (yellow) are shown as anisotropic/isotropic atomic displacement ellipsoids only to highlight the three-dimensional network for Li-ion conduction. Light pink circles represent tentative H positions. The 3-dimensional network for possible Li-diffusion is shown as a bond valence energy landscape map at a level of 1.0 eV above the minimum (blue-green contours).

Both Li-sites are only partly filled. This is discernible in the first refinement cycle. Here the electron density at both sites is modeled using the assumption that only Li occupies these sites. In this model, the Li1 site in the pristine sample is 67% full, and the Li2 site only 38% full. Interestingly, the electron density increases at the Li1 site with prolonged storage but decreases at Li2 site. As vacancies exist, Li^+ and Al^{3+} are assumed to occupy the regular tetrahedral sites, but it is impossible to independently determine the Al^{3+} content. A value of 0.1 apfu is used based on previous studies that used EDX analysis on analogous material [5,9], which was prepared under identical synthesis conditions: i.e., identical amounts of the same starting materials, same experimental setup, and procedure, etc. With all the Al^{3+} assigned to the Li1 site and its value fixed, the Li^+ content on both Li1 and Li2 sites can now be easily refined.

Assuming that the Al content at the tetrahedral sites does not change, the amount of Li^+ at the Li1 site slightly increases with increased aging during the first 300 days, while that

at the Li2 site distinctly decreases, as depicted in Figure 6. This is interpreted to be the result of a migration of ~0.5 apfu Li$^+$ from the Li2 to the Li1 site. Thereafter, there is no significant change. This means that the number of vacancies at 24*d* is significantly reduced. Modeling the electron density with only Li at the 96*h* site, the Li content decreases from ~4.5 apfu to ~2.8 apfu. Assuming that ~0.5 apfu migrates to the Li1 site, the remaining loss of 1.2 apfu Li is interpreted to be the result of the replacement of Li$^+$ by H$^+$, such that 1.2 apfu H$^+$ is incorporated in the LLZO structure during the 936 days of aging. As the same single crystal was used throughout, and the structural factors are measured to low values in d-space, and the presence of a consistent trend in the measured data, it is assumed that the observations are significant. However, the localization of the protons in the structure is hard to facilitate. As outlined by [17,24], the most probable position for *x*, *y*, and *z* is centered around 0.072, 0.235, and 0.325, respectively. In hydrogarnet ($Ca_3Al_2(O_4D_4)_3$), the deuterium atoms have *x*, *y*, and *z* positions of 0.0913, 0.2015, and 0.3483, respectively, as determined by Lager et al. [31] using time of flight neutron diffraction data. This is about 0.906 (1) Å away from the center of vacant 24*d* tetrahedral sites, with the OD vector pointing towards the empty site [31]. We found similar possible positions for Al10-LLZO that also point towards the only partially filled 24*d* site. However, the obtained OH vectors are rather short and the obtained occupation numbers tend to be too high and do not correlate with the expected H$^+$ contents. Nevertheless, as the best approximation, it is accepted that the H$^+$ ions are bonded to the O1 sites with the OH vector pointing towards the 24*d* site.
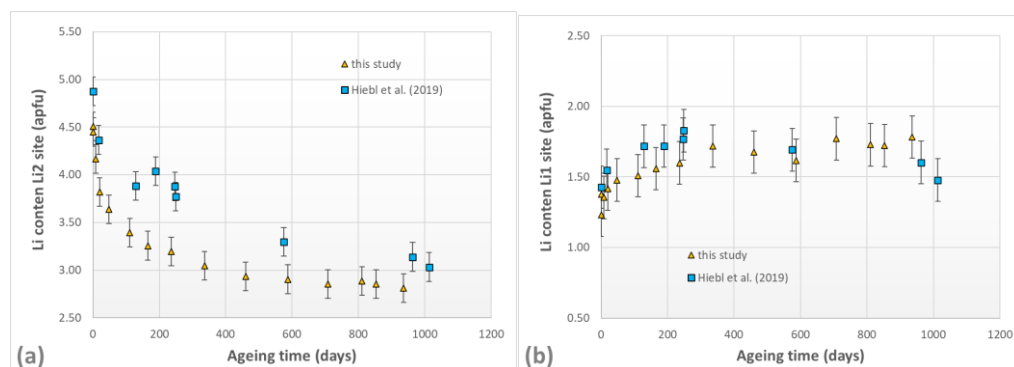

Figure 6. Variation of the Li-content at the Li1 (**a**) and Li2 (**b**) sites of Al10-LLZO during aging in a moist atmosphere. Note, the same crystal is used and remeasured.

The increase in lattice parameters with age, and associated cation migration and cation exchange reactions induce some rearrangements in the bonding topology. While, as expected, only very small alterations in La–O and Zr–O bond lengths are observed (small decreases within 2 estimated standard deviations), there is a significant increase of the Li1–O bond length (Figure 7a). This is accompanied by changes in the separation between Li-atoms at the Li1 and Li2 sites; i.e., the shorter interatomic distance increases from 1.904 (14) Å to 1.929 (15) Å whereas the longer one decreases from 2.398 (19) to 2.299 (14) Å. As Li1 resides in a special position, 24*d*, the changes in Li1–O bond lengths are due to shifts in the oxygen atom positions, which, in course, can be determined effectively using X-ray diffraction data. So, these changes in the bond length are true alterations of the LLZO structure in response to aging effects. The alterations in the Li2–O environment are even more pronounced. On average, the four closer Li2–O bond lengths increase from 2.097 (6) to 2.112 (7) Å whereas the more distal Li2–O bond length, in contrast, is reduced from 2.65 (2) to 2.60 (2) Å.
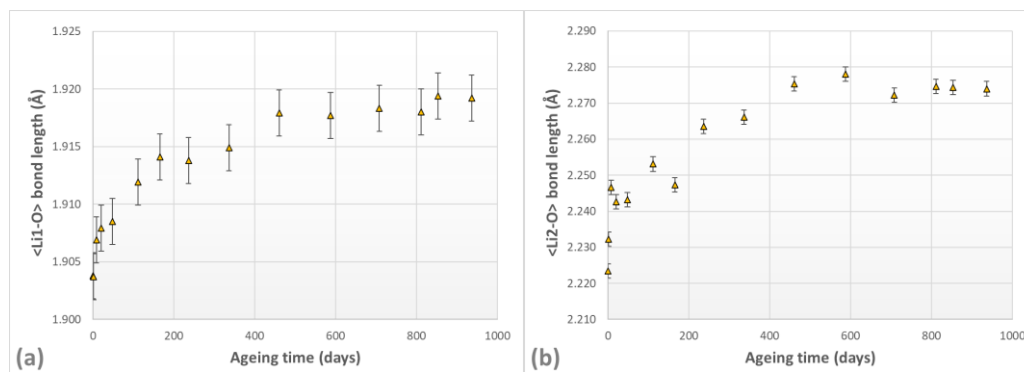
Figure 7. Variation of the average Li-O bond lengths at the (**a**) 24*d* (Li1) and (**b**) 96*h* (Li2) sites in Al10-LLZO during aging in a moist atmosphere. Note, the same crystal is used and remeasured.

To monitor the progress of hydration of Al-stabilized LLZO, aging experiments were performed under mild hydrothermal conditions at 90 °C using different residence times. Diffraction data from crystals treated for 1.75 days display no change in space group symmetry but show similar deep hydration after 936 days of exposure to moisture. After only 4-days, however, the expected symmetry reduction to $I\bar{4}3d$ symmetry is observed. Prolonged treatment of up to 9 days results in more deeply hydrated LLZO crystals.

The symmetry change is detectable by the presence of Bragg peaks with Miller indices of k = odd and l = odd. These peaks are forbidden in SG $Ia\bar{3}d$ but allowed in SG $I\bar{4}3d$. Such a reduction of symmetry has already been noted by some other authors [16,17,24], but this is the first time it is observed in Al-stabilized LLZO. This symmetry reduction induces several rearrangements within the atomic architecture. Zr^{4+} ions shift from (0, 0, 0) with site symmetry $\bar{3}$ in SG $Ia\bar{3}d$ to the 16*c* position (x, x, x) with site symmetry 3, thus allowing for two different Zr-O bond lengths in SG $I\bar{4}3d$. The oxygen atom sites split into the two 48*e* positions, O1 and O2, and, most importantly, the 24*d* tetrahedral site in SG $Ia\bar{3}d$ also splits into two different sites, 12*a* (Li1) and 12*b* (Li2) in $I\bar{4}3d$. Interstitial Li is now found at the general 48*e* position (Li3). The structure of highly Ga-stabilized LLZO was used as a starting model for refining the structure of Al10-LLZO with $I\bar{4}3d$ symmetry. Strong evidence is found that Al^{3+} occupies the 12*a* position: modeling the electron densities at the Li sites with Li only yields an overpopulation at the 12*a* site (Li1), while the other sites have the expected underpopulation. Thus, Al^{3+} was solely accommodated at the 12*a* site and its content was fixed again at 0.1 apfu. It is postulated that this ordering of Al^{3+} during increasing migration of Li^+ to the tetrahedral sites contributes to the phase transition, and allows for two different tetrahedral sites: one with the ordering of Al^{3+} and Li^+, the other with Li^+ only. For deeply hydrated samples, residual electron density analysis yields some positive peaks close to the O1 oxygen atom, but no clear indications for the presence of protons close to O2 were found, suggesting that H^+ is only bonded to the O1 oxygen atom. Independent refinements, however, suffer similar problems as outlined above.

The lattice parameters of the aged samples correlate well with the refined total Li^+ content (Figure 8). Some slight non-linear behavior within the $Ia\bar{3}d$ phase is observed that may be due to the cation migration from the 96*h* to 24*d* positions. The phase transition to $I\bar{4}3d$ occurs when Li^+ contents are between 4.2 and 4.5 apfu, corresponding to estimated H^+ contents of between 1.2 and 1.5 apfu. An increase in occupation of the tetrahedral 24*d* position was observed in the $Ia\bar{3}d$ phase during aging and increase of the lattice parameter. This trend is prolonged within the $I\bar{4}3d$ phase (sum of the occupation of 12*a* and 12*b* sites) but tends to stabilize at an occupation value of ~2.5 apfu. Thereby, 12*a* and 12*b* sites behave differently: while occupation at the 12*a* site steadily increases from 0.86 (2) apfu to 1.43 (2) apfu, thus obtaining almost full occupancy, that at the 12*b* site fluctuates around 1.00 apfu. Li^+ occupation of the interstitial 96*h* ($Ia\bar{3}d$) and 48*e* ($I\bar{4}3d$) positions is distinctly reduced. Consequently, it becomes very evident that replacement of Li^+ by H^+ takes place at the general interstitial sites, whereas the Li^+ in the regular tetrahedral sites of the garnet

structure seems to be more rigidly bonded and does not take part in the exchange reaction unless there is some Li$^+$ at the general 48e sites.
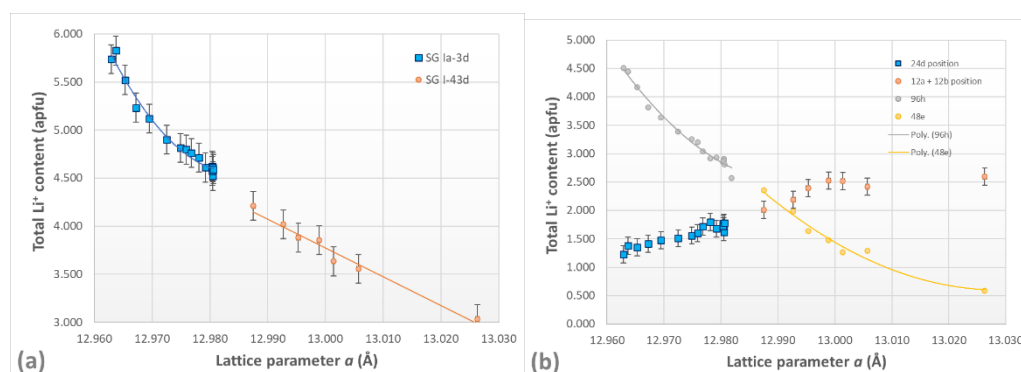

Figure 8. Variation of Li-site occupation in Al-stabilized LLZO garnets as a function of change in unit cell parameters during aging, from refinements of high-resolution X-ray diffraction data. (**a**) total Li content in the samples, (**b**) Li-content on the individual sites.

During the phase change of the $I\bar{4}3d$ phase, bond lengths change, and lattice parameters increase with increasing Li$^+$ replacement. There are two independent La–O bond lengths in the $Ia\bar{3}d$ phase (see Table 3); these split into four in the $I\bar{4}3d$ structure.

Figure 9a shows the changes in unit cell dimension for the shorter La–O bonds: while the phase change causes a distinct splitting of these bond lengths, they are stretched to a small extent towards the larger unit cell parameters during prolonged aging. The Zr–O bonds are more affected (Figure 9b). The bonds in $Ia\bar{3}d$ tend to decrease, but there is a district distortion of the octahedron during the phase change due to both a displacement of the oxygen atoms and a shift of the Zr^{4+} atom to the 16c position. Zr–O bond lengths start to change by ~0.04 Å on approaching the phase change and continue to change during further aging. The splitting of the tetrahedrally coordinated 24d position into two sites is also reflected in the bond lengths: the distance between Li1 (12a) -O1 sites increases while the bond with the Li2 site (12b) shrinks upon symmetry change. Highly charged doping cations seem to prefer the larger tetrahedral Li1 polyhedron. Within the $I\bar{4}3d$ phase, Li1–O1 and Li2–O2 bond lengths increase by 0.037 and 0.032 Å, respectively. Even if significantly greater estimated standard deviations than those applied to $Ia\bar{3}d$ are applied, the smooth and steady increase in values indicates that the changes are real. The average of four Li3–O distances of the interstitial Li atom (96h, 48e) also increases, whereby for individual bonds, the smaller distance between Li3 and the O1 oxygen atoms decreases from 1.916 (14) to 1.894 (14) Å. It is also observed that the Li1–Li3 interatomic distance increases whereas that between Li2 and Li3 decreases, i.e., the Li3 site moves closer to the Li2 site during aging. This is interpreted to be due to increasing repulsion due to the incorporation and bonding of H$^+$ to the O1 oxygen, and Li is shifted toward the non—hydrated O2 oxygen atoms of the Li2–O2 tetrahedron.

3.2.2. Structural Analysis of Ga- Stabilized LLZO

Ga-doping of LLZO triggers a transformation to the acentric $I\bar{4}3d$ structure even with small Ga^{3+}—contents of >0.08 apfu [7]. Its behavior during aging is mainly studied using a crystal with nominal composition Li$_{6.7}$La$_3$Zr$_2$Ga$_{0.1}$O$_{12}$ (Ga10-LLZO). This data is complemented with results from the second series of aging experiments on a crystal with nominal Li$_{5.8}$La$_3$Zr$_2$Ga$_{0.4}$O$_{12}$ composition (Ga40-LLZO). Note, due to a low data density in the early stage of aging, data from the aging of several other crystals of Ga40-LLZO from different charges are also included.
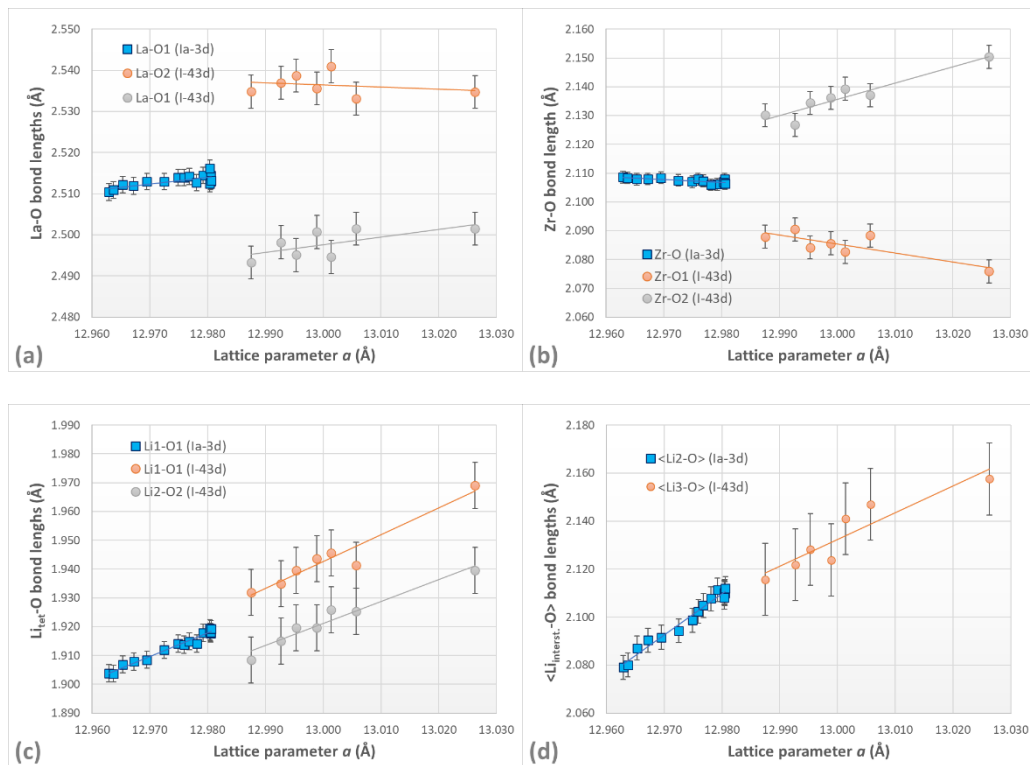
Figure 9. Variation of bond lengths in Al10-LLZO as a function of change in unit cell parameters with aging, from refinements of high-resolution X-ray diffraction data. (**a**) Smaller La–O bond lengths, (**b**) Zr–O bond length, (**c**) Li–O bond lengths at the regular tetrahedral sites (24*d*, 12*a*, and 12*b*), and (**d**) average Li–O bond lengths at the interstitial site (96*h* and 48*e*) assuming a 4-fold coordination of the site.

An $I\bar{4}3d$ symmetry is observed in all single-crystal X-ray diffraction measurements of Ga-stabilized LLZO in this study, independent of age and degree of hydration of the sample. There is also no difference evident between different Ga–LLZO samples (Ga10, Ga40). However, the unit cell does expand in all samples on exposure to ambient conditions or moisture (Figure 4b) but this observed increase, due to Li^+-H^+ exchange, is smaller than that in Al10-LLZO. Also, early-stage hydration seems to be slower and the increase in the unit cell less rapid than in Al10-LLZO; the reason for this could be, for example, due to the larger sizes of the single Ga-LLZO crystals, so diffusion rates would be lower.

In data evaluation, the refinement strategy is the same as that outlined in detail in [7]. Li^+ is distributed over three sites; Li1 and Li2 are on the two regular tetrahedral sites (12*a* and 12*b*, respectively), and Li3 is on the general position 48*e*. As for Al-LLZO, the electron densities at the Li sites in Ga40-LLZO were first modeled with Li-scattering factors only, and a distinct (Li1) and a very small (Li2) over-occupation is observed. Therefore, the stronger scattering ion, Ga^{3+}, should also be included in the modeling. Hence, in the second step of refinement, the Li1 and Li2 sites are assumed to be fully occupied with Li and Ga. The results show that Ga^{3+} has a strong preference for the Li1 site with 0.26 apfu Ga^{3+} at Li1 and ~0.01 apfu Ga^{3+} at the 12*b* site; this is in agreement with the findings of Wagner et al. [8]. The Li3 site is filled to ~61%. The situation is somewhat different for low nominal Ga^{3+} contents, i.e., for Ga10-LLZO. Here there is no overpopulation of the 12*b* site evident when Li^+ only is used to model the electron density at this site, but some vacancies are present. This is presented as strong evidence that no Ga^{3+} enters the 12*b* site. Also, the refined Ga^{3+} content at the 12*a* site increases over storage time, when the full occupation of this site is assumed and the scatter is modeled using Li + Ga = 1. An increasing Ga^{3+} content during storage time in a wet environment, however, is rather unrealistic. The Ga^{3+} content stabilizes at high storage time to values of ~0.12 apfu, which is used here for all measurements. Thus, the total cation occupation at Li1 was lowered accordingly so that

the Ga—content approaches this value, i.e., different amounts of vacancies are considered. The main results of these refinements are compiled in Figure 10.
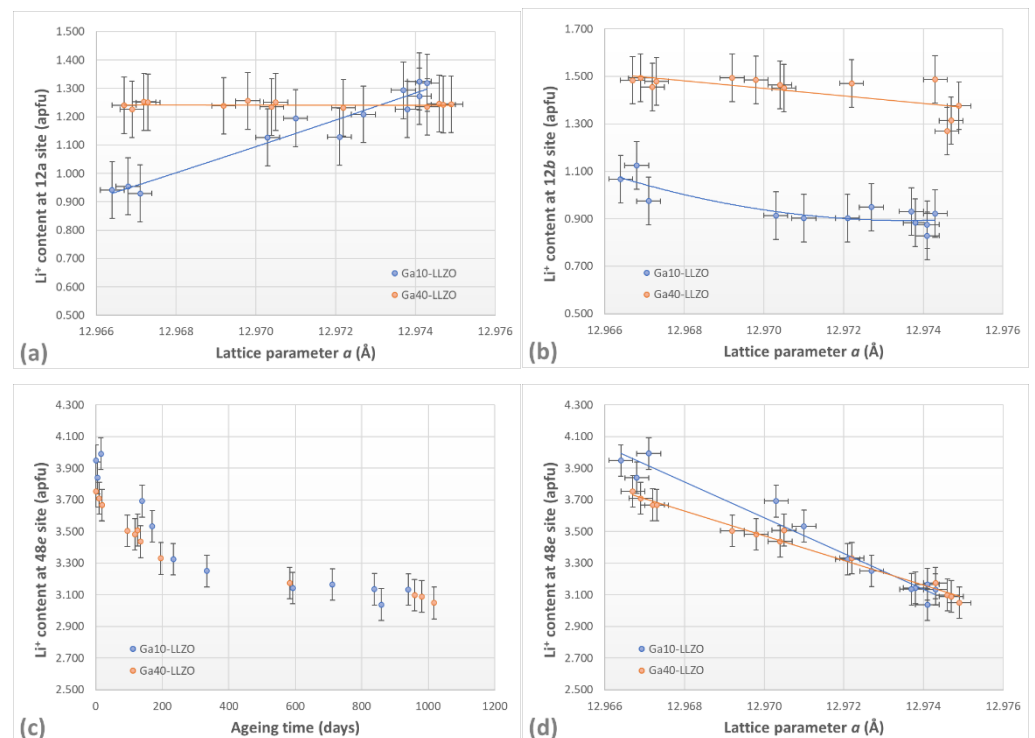

Figure 10. Variation of site occupation numbers in Ga-dopped LLZO as a function of lattice parameter (**a**,**b**,**d**) and storage time (**c**).

During aging, the Li^+ content at the 12*a* site (Li1) in Ga40-LLZO remains constant but in Ga10-LLZO, it steadily increases (Figure 10a) and the vacancy content decreases. This is in line with the observations of Al-stabilized LLZO, where occupation increases over time due to some migration of Li^+ to regular tetrahedral sites. The occupation of Li^+ in Ga40-LLZO is lower due to the higher Ga^{3+} content for this series of samples. It should be pointed out that the site occupation here is remarkably constant. There is a small loss of Li^+ (~0.2 apfu) from the 12*b* site during aging in moist air (Figure 10b). Refinements for Ga10-LLZO additionally reveal the distinct presence of a number of vacancies at this site, which further proves that cation ordering is responsible for symmetry reduction, and vacancies seem to order at 12*b*. This contrasts somewhat with the assumed full occupancy of this site in Ga40-LLZO. For long storage times, the whereabouts of Li+ are not fixed in the refinement but the Ga content is fixed to the value of the pristine material, and a small loss of Li^+ from 12*b* is observed. It cannot be excluded that there are more vacancies at 12*b*; e.g., increasing the Ga^{3+} content from the observed 0.02 to a fixed 0.05 apfu, reduces the total occupation at 12*b* to 70%, which is what is proposed for Ga10-LLZO. This would also bring the total Ga^{3+} content closer to the nominal content. This refinement is preferred here because it is based on fewer assumptions and it does not affect either the general fit of the data trend lines or any of the parameters other than the vacancy content on Li2.

Most important of all, refinements of the datasets indicate a significant decrease in electron density at the Li3 site over time. The loss is quick within the first period of aging and stabilizes at longer storage times in a wet environment (Figure 10c). Data indicate that Ga10-LLZO and Ga40-LLZO behave similarly. The loss of Li^+ from the interstitial 48*e* (Li3) site is ~1.2 apfu during aging under the specific experimental conditions; the lowest Li3 site occupation is around 3 apfu. The decrease in Li site occupation is almost linear when expressed as a function of change in unit cell parameters (Figure 10d). For charge balance, H^+ has to be incorporated and, as for Al-LLZO, is bonded to the O1 oxygen atom. Despite

independent refinements not being possible, around 1 apfu of H$^+$ has to be incorporated into the LLZO structure based on the assumption that some Li$^+$ migrates from 48e to 12a.

Hydrothermal treatment of Ga10-LLZO samples at 90 °C for 7, 14, and 28 days triggers much deeper hydration. Data from this experiment are presented in Tables 2–5. The 12a site maintains its occupation for up to 14 days of exposure, but then suffers Li$^+$ loss of between ~1.38 (5) and 0.95 (5) apfu. There is also a steady decrease in occupancy at the 12b site similar to that observed during aging in moist air. Li$^+$ is extracted from the 48e (Li3) site so that there is only 0.88 (6) apfu, thereafter, the 28-day treatment.

As observed for Al-LLZO, aging also induces some small alterations in the bonding topology in Ga-LLZO. The La–O2 bond lengths decrease slightly and the La–O1 bond lengths increase. These changes are only within two standard deviations but as they do define a steady trend, they are taken to reflect a real change. A similar picture is observed for the Zr–O bonds; the O2 oxygen bonds become shorter and those with the O1 oxygen atom expand but only minimally. Changes within the Li-ion coordination spheres are more evident. All Li-O bond lengths increase. This is most prominent when the four Li3–O bond lengths are averaged. The interatomic distance between the Li1 and Li3 sites significantly increases by ~0.028 (2) Å and that between Li2 and Li3 decreases by ~0.038 (6) Å. Again, this indicates that the Li3 site is displaced from the Li1 towards the Li2 atom, i.e., away from the tetrahedron that is coordinated by the O1 oxygen atom, which hosts the OH group. The expansion—even if on a very small level—of the Zr–O1 and La–O1 bonds could be interpreted to indicate the presence of protons around the O1 oxygen atom. For Ga10-LLZO, the full set of variations of structural parameters with unit cell parameter a is listed in Appendix A.

4. Discussion and Conclusions

Despite the enormous amount of research on LLZO, little is known on the structural modifications and cation distribution in the garnet structure during aging. Therefore, we have performed a comprehensive study of the Li$^+$-H$^+$ exchange reaction in Al- and Ga-stabilized LLZO under different wet-environmental conditions as a function of time (up to 936 days) using powder diffraction (for unit cell dimension determination of polycrystalline material) in combination with full structural analysis of single-crystal X-ray diffraction methods.

Fine-grained powder—exposed to ambient conditions—quickly shows an increase in its lattice parameters and Li$_2$CO$_3$ forms even at short exposure times in air, indicating a high sensitivity of Al- and Ga-stabilized LLZO to even low levels of moisture (<20% relative humidity). Monitoring the change in lattice parameters with time shows that Li$^+$-H$^+$ exchange is fast at the very beginning but becomes slower with time. A saturation value of a ~13.075 Å is observed for both Al- and Ga-stabilized LLZO and could be a measure of the maximum Li$^+$/H$^+$ exchange possible in LLZO within the environments tested. The uptake of H$^+$ into the crystal structure is confirmed by a weight loss of 4–6% detected above 350 °C in differential thermal analysis (DTA) of similarly highly-altered LLZO [23].

Exposure to a high humidity environment (saturated water pressure in a sealed desiccator at 22 °C) triggers the decomposition of the LLZO structure in both compositions, leading to the formation of crystalline La$_2$(CO$_3$)$_3$·8 H$_2$O and an amorphous material as well as another unidentified phase. This is consistent with results from previous studies on Li$_6$La$_3$ZrTaO$_{12}$ [24].

A more detailed insight into the mechanisms of aging is based on structural analysis. Cubic LLZO stabilized with Al contains Li$^+$ at both the regular tetrahedral 24d site and the interstitial 96h site. However, both sites have a high degree of vacancy. The electron density at the 24d site increases during storage in moist air over a period of 936 days, whereas that at the 96h site distinctly decreases over the same period. This strongly indicates that there is a remarkable loss of Li$^+$ at the 96h site accompanied by an uptake of H$^+$ and displacement of Li$^+$ to the partly unoccupied 24d site. With increasing hydration, occupation increases

with the ordering of Al^{3+} at the 24*d* site, inducing a symmetry reduction to $I\bar{4}3d$ that has not been reported so far in Al-stabilized LLZO but has been recently explored in $Li_6La_3ZrTaO_{12}$. Locating the protons was not fully possible, but they are probably bonded to the O1 oxygen and point towards 96*h* (in $Ia\bar{3}d$) or 48*e* (in $I\bar{4}3d$ space group), as reported in [17,18,31]. This is supported by the changes observed in bonding topology with a displacement of the Li3 site away from the Li1 site (coordinated by OH) towards the Li2 site (bonded solely to oxygen atoms).

Ga-stabilized LLZO shows $I\bar{4}3d$ symmetry in the pristine state. This composition was chosen to validate the observations already made for Al- stabilized LLZO. As discussed in detail in [8], Ga^{3+} has a preference for the larger 12*a* tetrahedral site, and the total vacancies in pristine Ga-LLZO are significantly less than within the $Ia\bar{3}d$ symmetry of Al-stabilized LLZO. As vacancies decrease significantly (by ~0.5 apfu) in Al-LLZO towards the transition to $I\bar{4}3d$, it may be concluded that increasing the occupation at the tetrahedral sites additionally promotes the symmetry reduction in LLZO type garnets. During the aging of Ga-LLZO in moist air, the 12*b* site shows almost constant occupation, while 48*e* loses significant Li^+. Deep hydration under mild hydrothermal conditions promotes extraction of Li^+ from 48*e* and reduces its value from ~4.0 apfu in the pristine samples to ~1.0 apfu in altered samples. Studies on hydrothermally-treated single crystals also show a loss of Li^+ on the 12*b* sites. In contrast, the occupation of the 12*a* sites remains almost unchanged, probably due to the presence of Ga^{3+}, which can hinder the extraction of Li from the 12*a* sites.

Charge balance is also maintained in Ga-LLZO by the incorporation of protons, which are bonded to the O1 oxygen atom. There is no indication for a residual electron density close to the O2 oxygen atom. Cation distribution and exchange in Ga- stabilized LLZO strongly support the results determined for Al- stabilized LLZO.

Overall, this study shows that high-resolution single-crystal X-ray diffraction-based structural analysis can yield important insights into the structural degradation mechanisms of battery-related materials, even for low scattering elements such as Li^+.

Author Contributions: Conceptualization, G.J.R. and D.R.; synthesis, A.P.; X-ray diffraction, G.J.R. and G.T.; validation, G.J.R., and G.T.; investigation, G.J.R., G.T.; data curation, G.J.R.; writing—original draft preparation, G.J.R. and D.R.; writing—review and editing, G.J.R. and D.R.; visualization, G.J.R. All authors have read and agreed to the published version of the manuscript.

Institutional Review Board Statement: Not applicable.

Informed Consent Statement: Not applicable.

Data Availability Statement: Additional data may be requested from the first author.

Conflicts of Interest: The authors declare no conflict of interest.

Appendix A

Variation of bond lengths in Ga10-LLZO as a function of change in unit cell parameters due to ongoing aging, from refinements of high-resolution X-ray diffraction data.
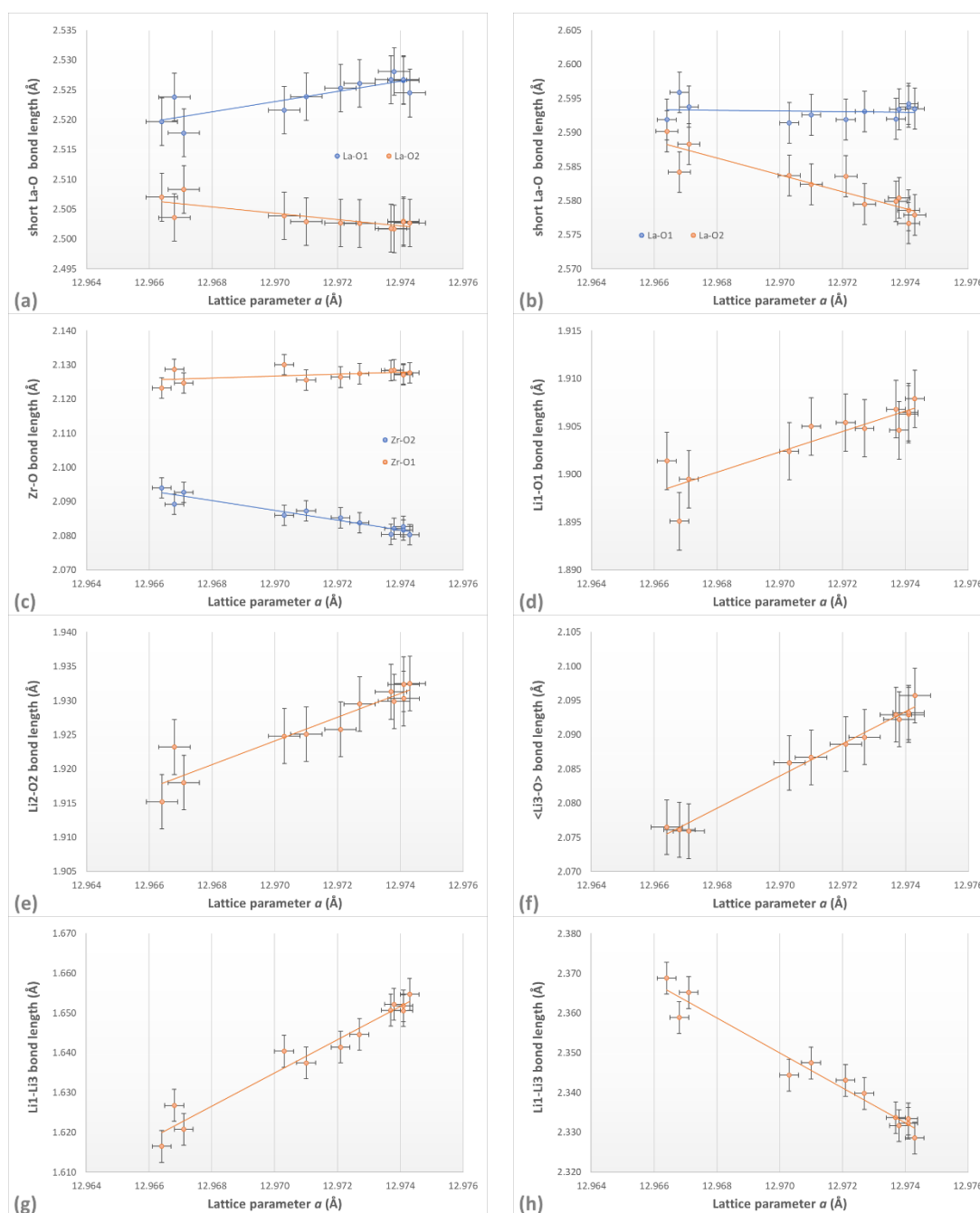
Figure A1. Variation of bond lengths in Ga10-LLZO with the unit cell parameters due to ongoing aging (Li$^+$/H$^+$ exchange), data extracted from refinements of high-resolution single-crystal X-ray diffraction data: (**a**) Variation of the two short La–O bond lengths, (**b**) variation of the two long La–O bond lengths, (**c**) variations of the two different Zr–O bond lengths, (**d**) variations of the Li1–O1 bond lengths, (**e**) variations of the Li2–O2 bond lengths, (**f**) variations of the average Li3–O bond lengths, based on the 4 shortest bonds, (**g**) variation of the interatomic separation of Li1–Li3 sites and (**h**) variation of the interatomic separation of Li2–Li3 sites with lattice parameter *a*.

References

1. Ramakumar, S.; Deviannapoorani, C.; Dhivya, L.; Shankar, L.S.; Murugan, R. Lithium garnets: Synthesis, structure, Li$^+$ conductivity, Li$^+$ dynamics and applications. *Prog. Mater. Sci.* **2017**, *88*, 325–411. [CrossRef]
2. Wang, C.; Fu, K.; Kammampata, S.P.; McOwen, D.W.; Samson, A.J.; Zhang, L.; Hitz, G.T.; Nolan, A.M.; Wachsman, E.D.; Mo, Y.; et al. Garnet-Type Solid-State Electrolytes: Materials, Interfaces, and Batteries. *Chem. Rev.* **2020**, *120*, 4257–4300. [CrossRef]
3. Buschmann, H.; Dolle, J.; Berendts, S.; Kuhn, A.; Bottke, P.; Wilkening, M.; Heitjans, P.; Senyshyn, A.; Ehrenberg, H.; Lotnyk, A.; et al. Structure and dynamics of the fast lithium ion conductor "Li$_7$La$_3$Zr$_2$O$_{12}$". *Phys. Chem. Chem. Phys.* **2011**, *13*, 19378–19392. [CrossRef]
4. Awaka, J.; Kijima, N.; Hayakawa, H.; Akimoto, J. Synthesis and structure analysis of tetragonal Li$_7$La$_3$Zr$_2$O$_{12}$ with the garnet-related type structure. *J. Solid State Chem.* **2009**, *182*, 2046–2052. [CrossRef]
5. Rettenwander, D.; Geiger, C.A.; Tribus, M.; Tropper, P.; Amthauer, G. A Synthesis and Crystal Chemical Study of the Fast Ion Conductor Li$_{7-3x}$Ga$_x$La$_3$ Zr$_2$O$_{12}$ with x = 0.08 to 0.84. *Inorg. Chem.* **2014**, *53*, 6264–6269. [CrossRef]
6. Rettenwander, D.; Wagner, R.; Langer, J.; Maier, M.E.; Wilkening, M.; Amthauer, G. Crystal chemistry of Li$_7$La$_3$Zr$_2$O$_{12}$ garnet doped with Al, Ga, and Fe: A short review on local structures as revealed by NMR and Mossbauer spectroscopy studies. *Eur. J. Mineral.* **2016**, *28*, 619–629. [CrossRef]
7. Wagner, R.; Redhammer, G.J.; Rettenwander, D.; Senyshyn, A.; Schmidt, W.; Wilkening, M.; Amthauer, G. Crystal Structure of Garnet-Related Li-Ion Conductor Li$_{7-3x}$Ga$_x$La$_3$Zr$_2$O$_{12}$: Fast Li-Ion Conduction Caused by a Different Cubic Modification? *Chem. Mater.* **2016**, *28*, 1861–1871. [CrossRef]
8. Wagner, R.; Redhammer, G.J.; Rettenwander, D.; Tippelt, G.; Welzl, A.; Taibl, S.; Fleig, J.; Franz, A.; Lottermoser, W.; Amthauer, G. Fast Li-Ion-Conducting Garnet-Related Li$_{7-3x}$Fe$_x$La$_3$Zr$_2$O$_{12}$ with Uncommon I4-3d Structure. *Chem. Mater.* **2016**, *28*, 5943–5951. [CrossRef] [PubMed]
9. Rettenwander, D.; Redhammer, G.; Preishuber-Pflugl, F.; Cheng, L.; Miara, L.; Wagner, R.; Welzl, A.; Suard, E.; Doeff, M.M.; Wilkening, M.; et al. Structural and Electrochemical Consequences of Al and Ga Cosubstitution in Li$_7$La$_3$Zr$_2$O$_{12}$ Solid Electrolytes. *Chem. Mater.* **2016**, *28*, 2384–2392. [CrossRef]
10. Wagner, R.; Rettenwander, D.; Amthauer, G. 1. Lithium ion–conducting oxide garnets. *Highlights Appl. Mineral.* **2017**, 3–22. [CrossRef]
11. Murugan, R.; Thangadurai, V.; Weppner, W. Fast Lithium Ion Conduction in Garnet-Type Li$_7$La$_3$Zr$_2$O$_{12}$. *Angew. Chem. Int. Ed.* **2007**, *46*, 7778–7781. [CrossRef] [PubMed]
12. Wang, Y.X.; Lai, W. Phase transition in lithium garnet oxide ionic conductors Li$_7$La$_3$Zr$_2$O$_{12}$: The role of Ta substitution and H$_2$O/CO$_2$ exposure. *J. Power Sources* **2015**, *275*, 612–620. [CrossRef]
13. Nyman, M.; Alam, T.M.; McIntyre, S.K.; Bleier, G.C.; Ingersoll, D. Alternative Approach to Increasing Li Mobility in Li-La-Nb/Ta Garnet Electrolytes. *Chem. Mater.* **2010**, *22*, 5401–5410. [CrossRef]
14. Ma, C.; Rangasamy, E.; Liang, C.; Sakamoto, J.; More, K.L.; Chi, M. Excellent Stability of a Lithium-Ion-Conducting Solid Electrolyte upon Reversible Li$^+$/H$^+$ Exchange in Aqueous Solutions. *Angew. Chem. Int. Ed.* **2015**, *54*, 129–133. [CrossRef] [PubMed]
15. Brugge, R.H.; Hekselman, A.K.O.; Cavallaro, A.; Pesci, F.M.; Chater, R.J.; Kilner, J.A.; Aguadero, A. Garnet Electrolytes for Solid State Batteries: Visualization of Moisture-Induced Chemical Degradation and Revealing Its Impact on the Li-Ion Dynamics. *Chem. Mater.* **2018**, *30*, 3704–3713. [CrossRef]
16. Galven, C.; Fourquet, J.-L.; Crosnier-Lopez, M.-P.; Le Berre, F. Instability of the Lithium Garnet Li$_7$La$_3$Sn$_2$O$_{12}$: Li$^+$/H$^+$ Exchange and Structural Study. *Chem. Mater.* **2011**, *23*, 1892–1900. [CrossRef]
17. Larraz, G.; Orera, A.; Sanjuan, M.L. Cubic phases of garnet-type Li$_7$La$_3$Zr$_2$O$_{12}$: The role of hydration. *J. Mater. Chem. A* **2013**, *1*, 11419–11428. [CrossRef]
18. Orera, A.; Larraz, G.; Rodríguez-Velamazán, J.A.; Campo, J.; Sanjuán, M.L. Influence of Li$^+$ and H$^+$ Distribution on the Crystal Structure of Li$_{7-x}$H$_x$La$_3$Zr$_2$O$_{12}$ (0 ≤ x ≤ 5) Garnets. *Inorg. Chem.* **2016**, *55*, 1324–1332. [CrossRef] [PubMed]
19. Novak, G.A.; Gibbs, G.V. Crystal chemistry of silicate garnets. *Am. Mineral.* **1971**, *56*, 791–825.
20. Uhlenbruck, S.; Dellen, C.; Möller, S.; Lobe, S.; Tsai, C.-L.; Finsterbusch, M.; Bram, M.; Guillon, O. Reactions of garnet-based solid-state lithium electrolytes with water—A depth-resolved study. *Solid State Ion.* **2018**, *320*, 259–265. [CrossRef]
21. Galven, C.; Dittmer, J.; Suard, E.; Le Berre, F.; Crosnier-Lopez, M.-P. Instability of Lithium Garnets against Moisture. Structural Characterization and Dynamics of Li$_{7-x}$H$_x$La$_3$Sn$_2$O$_{12}$ and Li$_{5-x}$H$_x$La$_3$Nb$_2$O$_{12}$. *Chem. Mater.* **2012**, *24*, 3335–3345. [CrossRef]
22. Liu, X.; Chen, Y.; Hood, Z.D.; Ma, C.; Yu, S.; Sharafi, A.; Wang, H.; An, K.; Sakamoto, J.; Siegel, D.J.; et al. Elucidating the mobility of H$^+$ and Li$^+$ ions in (Li$_{6.25-x}$H$_x$Al$_{0.25}$)La$_3$Zr$_2$O$_{12}$ via correlative neutron and electron spectroscopy. *Energy Environ. Sci.* **2019**, *12*, 945–951. [CrossRef]
23. Yow, Z.F.; Oh, Y.L.; Gu, W.Y.; Rao, R.P.; Adams, S. Effect of Li$^+$/H$^+$ exchange in water treated Ta-doped Li$_7$La$_3$Zr$_2$O$_{12}$. *Solid State Ion.* **2016**, *292*, 122–129. [CrossRef]
24. Redhammer, G.J.; Badami, P.; Meven, M.; Ganschow, S.; Berendts, S.; Tippelt, G.; Rettenwander, D. Wet-Environment-Induced Structural Alterations in Single- and Polycrystalline LLZTO Solid Electrolytes Studied by Diffraction Techniques. *ACS Appl. Mater. Interfaces* **2021**, *13*, 350–359. [CrossRef]
25. Hiebl, C.; Young, D.; Wagner, R.; Wilkening, H.M.R.; Redhammer, G.J.; Rettenwander, D. Proton Bulk Diffusion in Cubic Li$_7$La$_3$Zr$_2$O$_{12}$ Garnets as Probed by Single X-ray Diffraction. *J. Phys. Chem. C* **2019**, *123*, 1094–1098. [CrossRef]

26. Bruker. *Topas V4.1 (Version 2012)*; Bruker AXS Inc.: Madison, WI, USA, 2012.
27. Bruker. *APEX3 (Version 2015. 10-0)*; Bruker AXS Inc.: Madison, WI, USA, 2015.
28. Sheldrick, G. Crystal structure refinement with SHELXL. *Acta Crystallogr. Sect. C* **2015**, *71*, 3–8. [CrossRef] [PubMed]
29. Farrugia, L. WinGX and ORTEP for Windows: An update. *J. Appl. Crystallogr.* **2012**, *45*, 849–854. [CrossRef]
30. Kun, R.; Langer, F.; Delle Piane, M.; Ohno, S.; Zeier, W.G.; Gockeln, M.; Colombi Ciacchi, L.; Busse, M.; Fekete, I. Structural and Computational Assessment of the Influence of Wet-Chemical Post-Processing of the Al-Substituted Cubic $Li_7La_3Zr_2O_{12}$. *ACS Appl. Mater. Interfaces* **2018**, *10*, 37188–37197. [CrossRef] [PubMed]
31. Lager, G.A.; Armbruster, T.; Faber, J. Neutron and X-ray diffraction study of hydrogarnet $Ca_3Al_2(O_4H_4)_3$. *Am. Mineral.* **1987**, *72*, 756–765.